A facile hydrothermal reflux synthesis of $Ni(OH)_2$/GF electrode for supercapacitor application

A.A. Khaleed[1,2], A. Bello[1], J. K. Dangbegnon[1], F.U. Ugbo[1], F. Barzegar[1], D. Y. Momodu[1], J. Madito[1], T Masikhwa[1], O. Olaniyan[1], N. Manyala*[1]

[1]Physics Department, Institute of Applied Materials, SARCHI Chair in Carbon Technology and Materials, University of Pretoria, Pretoria 0028, South Africa.

[2]Physics Department, Ahmadu Bello University, Zaria, Nigeria.

*Corresponding author: N. Manyala (manyalancholu@gmail.com)

Abstract

$Ni(OH)_2$/graphene foam (GF) electrode was synthesized for electrochemical application by a facile hydrothermal reflux technique. The results obtained from the scanning electron microscopy showed that the $Ni(OH)_2$ spheres successfully coated the entire surface area of the GF. Specific capacitance of 2420 F g^{-1} at a current density of 1 A g^{-1} was obtained for $Ni(OH)_2$/GF composite electrode, as well as a capacitance retention of ~93% after 1000 charge-discharge cycles, demonstrating excellent cycle stability in 6.0 M KOH electrolyte. These results suggest that the composite could be a potential active material for high performance electrochemical applications.

Introduction

One of the greatest scientific and engineering problems is the actualization of a highly efficient energy conversion and storage systems [1–3]. Electrochemical capacitors also known as supercapacitors or ultracapacitors have become attractive and suitable in energy storage systems due to their excellent power performance, reasonable energy density, as well as good cycle life [4,5]. Electrochemical capacitors are classified as Electrochemical double layer capacitors (EDLC) that use reversible adsorption/desorption of ion at the surface of the active materials, e.g. carbon materials with high specific surface area, and pseudocapacitors that store energy based on rapid surface redox reactions at or near surface of the active materials, which use among others conducting polymers and metal oxides/hydroxides compounds as active materials [6,7]. Hence, the electrochemical performance of supercapacitors depend on the type of active materials used, e.g. conducting polymers, transition metal oxides and hydroxides, and carbon materials [4,8]. Furthermore, the distinctive dimensions of the active materials are well essential for Electrochemical capacitors performance, considering the fact that the square of the diffusion distance is proportionate to the diffusion time of electrolyte ions [9,10]. In this regard, a considerable efforts have been focused on preparation of small size, porous, thin, hollow spheres materials with exposure of sufficient active sites and small diffusion length for enhancing electrochemical performance [11,12]. $Ni(OH)_2$ has been identified as an interesting transition metal hydroxides materials due to its easy production, low cost and great theoretical capacitance [13,14]. Thus, the preparation of the nanoscale $Ni(OH)_2$ for energy storage applications has attracted many attentions. Nonetheless, the nanoscale particles can agglomerate into big pieces or bulk, especially when the particle is under 10 nm, owing to their

high boundary energy [15]. Hence, employing nanoscale faradaic materials for electrochemical application is highly challenging.

Generally, combining a transition metal oxides (TMOs) or hydroxides (TMHOs) materials with the highly conductive materials is one of the techniques to stop accumulation and increase the conductivity [16,17]. For example, graphene is one of the commonly used material as substrate for composites, mostly due to the atom thick two-dimensional structure, high theoretical specific surface area of 2630 $m^2 g^{-1}$, high conductivity and good mechanical properties [13,14].

In spite of the many techniques that have been used to produce graphene nanocomposite electrodes, the agglomeration and assembling between graphene sheets owing to the strong π-π bonds remarkably compromise the large specific surface area of graphene [18,19]. Additionally, the presence of defects and chemical groups in reduced graphene oxide (rGO) along with the inter-sheet contact resistance affect the electrical conductivity of the composites [20]. Recently, three-dimensional (3D) graphene foam prepared via chemical vapor deposition (CVD) technique, which has a 3D macroscopic structure containing high-quality interconnected graphene and has a much higher electrical conductivity (10 *S/cm*) than chemically derived graphene could ease some of the problems mentioned above [21]. Liu *et. al.* have shown that ultra-small RGO-$Ni(OH)_2$ composites has high specific capacitance of 1717 F g^{-1} at 0.5 A g^{-1} [4]. Jiang *et. al.* found $Ni(OH)_2$ nanoflakes on 3D graphene by hydrothermal synthesis and achieved a large specific capacitance of 1450 F g^{-1} at 0.5 A g^{-1} [6]. Furthermore, Liu *et. al.* reported $Ni(OH)_2$-graphene sheet-carbon nanotube composite with specific capacitance of 1170.38 F g^{-1} at a current density of 0.2 A g^{-1} [22]. Gu *et. al.* recorded a specific capacitance of 1724 F g^{-1} at 2 A g^{-1} obtained from $Ni(OH)_2$ deposited on the silicon carbide nanowires by electrochemical

cathodic deposition [23] and Patil *et. al.* synthesized $Ni(OH)_2$ nanorod on graphene foam demonstrating a specific capacitance of 1139 F g^{-1} at 10 A g^{-1} [24].

In this article, we report on the facile hydrothermal reflux synthesis of $Ni(OH)_2$ on GF to produce $Ni(OH)_2$/GF by taking advantage of the synergy between the two materials. The $Ni(OH)_2$/GF electrode showed an excellent specific capacitance of ~2420 $Fg^{-1}$and good Coulombic efficiency (ε) after 1000 cycles in a cycling test.

Experimental

Synthesis of $Ni(OH)_2$/GF

Atmospheric pressure chemical vapor deposition (AP-CVD) growth system was employed to synthesize graphene foam (GF) on a nickel foam (NF) template (from Alantum, Munich, Germany with an areal density of 420 g m^{-2} and 1.6mm thickness). The synthesis was reported in our previous work [25]. Briefly, the NF was loaded at the center of a quartz reactor which was heated up to 1000 $^{\circ}$C under Ar:H_2 gas ratio of 300:200 sccm. Once the desired temperature is attained i.e, the 1000 $^{\circ}$C, it is kept constant for 60 minutes in order to remove the oxide layers and impurities on the NF before introduction of the carbon source (CH_4 gas) at the same temperature. 10 sccm of CH_4 (carbon source) was added to the previous gas ratio for 5 minutes. The quartz reactor chamber was then pushed immediately to a lower temperature region to help rapidly cool the sample which consists of graphene deposited on NF. Finally, GF was obtained by etching away the nickel template in a hot 3.0 M HCl solution at 60 °C, for several hours. Subsequently, the floating GF was continuously washed with deionized water and finally dried at 60 $^{\circ}$C in an electrical oven.

$Ni(NO_3).6H_2O$ (0.32 mol) and urea (1.28 mol) were dissolved in 160 ml of deionized water. The next step involved addition of 20 mg of GF to the above mixture and sonicated for 12 h, followed by subsequent stirring for 15 minutes to ensure homogeneous dispersion of GF in the solution. The mixture was then transferred into 250 ml flask with a reflux condenser, which was then dipped in an oil bath and followed by heating at 150 $^{\circ}$C and continuous magnetic stirring for 2 h. The flask was then removed from the oil bath and cool down naturally. The resulting greenish precipitate was centrifuged and washed continuously with deionized water prior to drying at 80 $^{\circ}$C for 12 h in an electrical oven. For comparison with the above prepared composite, pure $Ni(OH)_2$ was synthesized using the similar procedure without addition of GF.

Material Characterization

Raman spectroscopy was used to study the vibrational modes of the materials synthesized using a Jobin Yvon Horiba TX 6400 micro-Raman spectrometer. A 514 nm of an Ar ion laser was used as excitation source with a power of 1.5 mW focused on the sample. Field emission scanning electron microscopy (FE-SEM) (high resolution Zeiss Ultra Plus 55) operating at 2.0 kV was used to characterize the morphology of the samples. XPERT-PRO diffractometer (PANalytical BV, Netherlands) in a Θ/2Θ configuration, with a cobalt tube at 35 kV and 50 mA, as X-ray source was utilized to study the crystallinity of the samples. Fourier transform infrared (FT-IR) spectra (Bruker Vertex 77 v FT-IR spectrometer) was used as a complementary vibrational mode study of the samples. The electrochemical properties of the different samples were examined with a Bio-Logic VMP300 workstation (Knoxville TN 37,930, USA) in a three-electrode configuration. In this configuration, the $Ni(OH)_2$/GF composite sample was the working electrode in a 6.0 M potassium hydroxide (KOH) electrolyte; Ag/AgCl (3 M KCl) as the

reference electrode and glassy carbon plate was the counter electrode. The cyclic voltammetry (CV) tests were performed in the potential window of 0 - 0.5 V (vs. Ag/AgCl, 3 M KCl) at different sweep rates in the range of 5-50 mV s^{-1}. The galvanostatic charge–discharge (CD) tests were also done at different current densities range of 1-20 A g^{-1} and the electrochemical impedance spectroscopy (EIS) tests were done in an open circuit and frequency range of 10 mHz–100 kHz.

Results and Discussion

Raman analysis of GF

The as synthesized GF was characterized with Raman spectroscopy to ascertain the existence of graphene in the sample. Figure 1 displays that the Raman spectrum of the GF contains of two

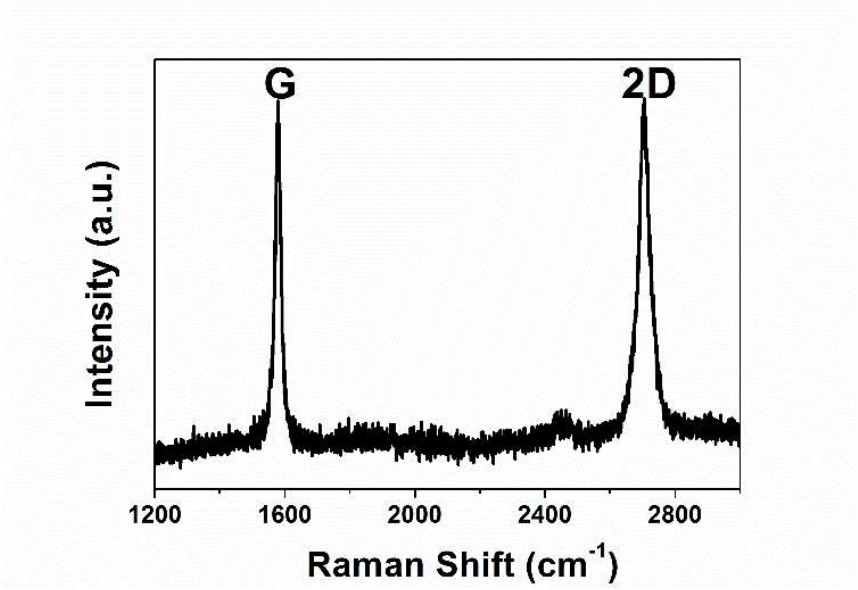

Fig. 1. Raman spectrum of the GF.

major peaks at 1580 cm^{-1} and 2704 cm^{-1} allocated to G and 2D modes of graphene, respectively. This indicates that the GF is of low defect density and good quality, due to the absence of the D-peak (which normally account for defect or disorder) at 1350 cm^{-1} [26].

Morphological and structural analysis

Fig. 2 shows low and high magnification images of $Ni(OH)_2$ and $Ni(OH)_2$/GF. Flake like $Ni(OH)_2$ spheres were observed at low and high magnification FESEM images (Fig 2a and b). $Ni(OH)_2$ sphere formation could be explained based on coalescence mechanism (an oriented attachment mechanism) and Oswald-ripening mechanism as in the following reactions [19,27]:

$$CO(NH_2)_2 + H_2O \leftrightarrow 2NH_3 + CO_2 \quad (1)$$

$$Ni^{2+} + x\,NH_3 \leftrightarrow [Ni(NH_3)_x]^{2+} \quad (2)$$

$$NH_3 + H_2O \leftrightarrow OH^- + NH_4^+ \quad (3)$$

$$Ni^{2+} + 2OH^- \leftrightarrow Ni(OH)_2 \quad (4)$$

Firstly, the process involved decomposition of urea to NH_3 and CO_2 (Equation 1). Then, NH_3 formed complexes with Ni^{2+}that reduces the amount of free Ni^{2+} and accordingly decreases the growth rate of the crystals [19,28]. According to Equation 1 and 3, urea can deliver a steady OH^- ion supply by hydrolysis during the hydrothermal reflux process. This is in favor of the formation and nucleation of $Ni(OH)_2$ nanoparticles depending on the coalescence mechanism. In thermodynamics viewpoint, the individual $Ni(OH)_2$ nanoparticle has extraordinary high surface energy. As the reaction continues further, the overall surface energy is minimized and therefore, the $Ni(OH)_2$ nanoparticles come together to form $Ni(OH)_2$ sphere [19,28]. Figs. 2c and

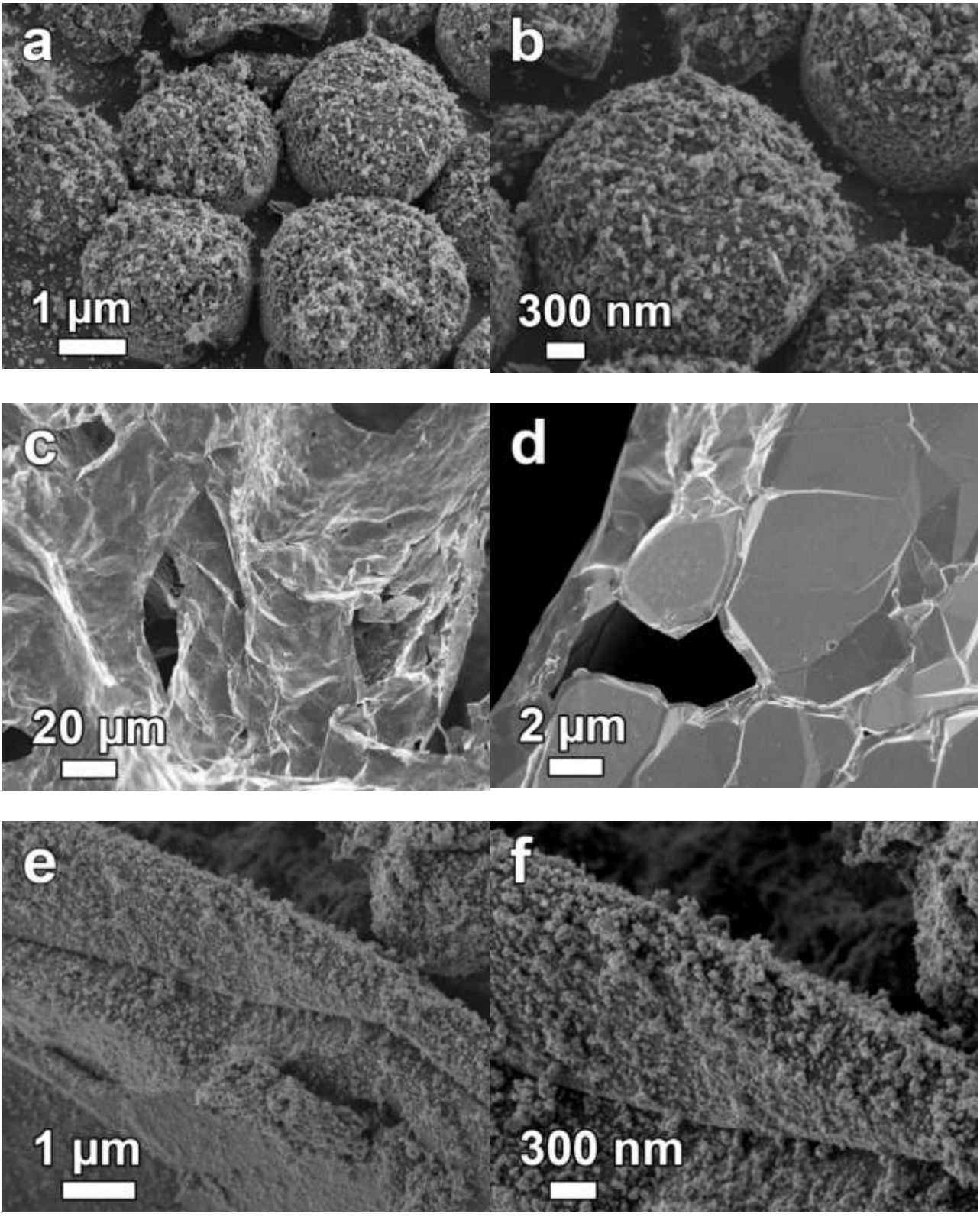

Fig. 2. (a) low magnification FESEM image of the pristine Ni(OH)2, (b) high magnification FESEM image of the pristine Ni(OH)2, (C) low magnification FESEM image of GF, (d) high magnification FESEM image of GF, (e) low magnification FESEM image of Ni(OH)2/GF , and (f) high magnification FESEM image of Ni(OH)2/GF.

2d show the low and high magnification micrographs of the GF. Fig. 2c shows the three dimensional structure of the graphene which was similar to the nickel template. Higher magnification image (Fig. 2d) shows that the surface of the GF contains of ripples and wrinkles because of the difference in thermal expansion coefficients of graphene and Ni in the CVD synthesis [29]. These wrinkles on the surface of the GF observed indicate that GF can serve as an ideal substrate to support $Ni(OH)_2$ spheres. SEM images of the composite material are shown in Figs. 2e and 2f for different magnifications indicating that the $Ni(OH)_2$ spheres successfully coated the entire surface area of the GF, therefore developing a porous and electro-conductive network structure. The morphology seen from FESEM results of the composite indicates that it is ideal for electrochemical applications because of the conductivity of GF and porosity of the $Ni(OH)_2$ in the composite, which could improve the capacitive behavior of the electrode.

XRD patterns of as synthesized pure $Ni(OH)_2$ and $Ni(OH)_2$/GF are presented in Fig. 3a. Indexed $Ni(OH)_2$ corresponding to diffraction pattern of rhombohedral α-$Ni(OH)_2$ (JCPDS No. 38-715) is observed [19,30]. The four distinctive peaks at 14.08°, 28.5°, 39.4° and 70.44° are assigned to (003), (006), (101), and (110) planes, respectively. Furthermore, similar XRD diffraction patterns are observed for both materials with only an additional weak peak appearing at 30.9° in the composite material. This weak peak is tentatively assigned to the (002) plane of graphene. However, a shift in 2θ values of these peaks are noticed as a result of the type of source used, e.g. peak from (003) plane which is a strongest diffraction peak commonly assigned to the 2θ value of ~ 12.1° [19,30] is now observed at 14.08°. Similarly, peaks shift exist for other planes, e.g. planes at (006), (101), (110) and (002), representing peaks at 2θ angle of 28.5°, 39.4°,

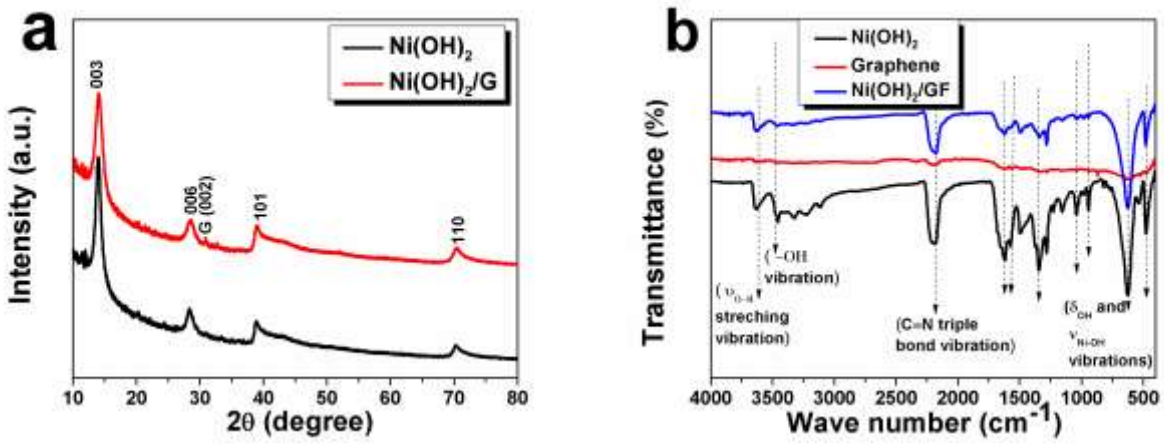

Fig. 3. (a) XRD diffraction and (b) FTIR spectra of the $Ni(OH)_2$, GF and $Ni(OH)_2$/GF samples.

70.44° and 30.9°, respectively. The slight shift in the diffraction pattern when compared to diffraction pattern with Cu as excitation source is due to the difference in wavelength of Co and Cu. Co, having longer wavelength will give rise to diffraction pattern at higher Bragg's angles. Moreover, XRD collected with a Co source permits the observation of low angle diffraction peaks with higher peak separation unlike when Cu is used [31,32]. Diffraction peak (003) plane has a stronger intensity than the others, showing that (003) plane may be the preferred growth direction. From Sherrer's equation, the average grain size calculated from the most intense diffraction peak (003) are 15.07 nm and 11.11 nm for $Ni(OH)_2$ and $Ni(OH)_2$/GF samples, respectively.

Fig. 3b shows the FTIR spectra of $Ni(OH)_2$, GF and $Ni(OH)_2$/GF in a wavenumber range of 400-4000 cm^{-1}. $Ni(OH)_2$ and $Ni(OH)_2$/GF have many similar vibration peaks as illustrated in the figure with the dotted lines. Peak at 3634 cm^{-1} is assigned to the υ_{O-H} stretching vibration [33], and the absorption band at 3458 cm^{-1} is attributed to –OH vibration of hydrogen-bonded hydroxyl groups from the $Ni(OH)_2$ [33,34]. The strong absorption band at 2181 cm^{-1} is attributed to the

vibration of C≡N triple bond in the OCN^{-1}, resulting from by-product of urea hydrolysis [35]. However, the C≡N triple bond in the composite coincides with the position of the C-H vibrations of the methylene group in GF spectrum [32]. However, the C≡N triple bond in the composite coincides with the position of the C-H vibrations of the methylene group in GF spectrum [32]. The intensity of C≡N triple bond in $Ni(OH)_2$ spectrum is very strong compared with that of C-H band in GF spectrum, resulting in weak peak in the composite due to the suppression of C-H band by the C≡N triple bond. The absorption band at 1618 cm^{-1} is related to the bending mode of interlayer water molecules, whereas the peaks at 1498 and 1043 cm^{-1} could be attributed to the existence of carbonate ions [35,36]. The band at 1342 cm^{-1} corresponds to the vibration of NO_3^- anion with D_{3h} symmetry in the interlayer space [33]. The band at 1282 and 945 cm^{-1} are associated to the vibration mode C-N bond [30], and the two peaks at 623 and 478 cm^{-1} correspond to the δ_{OH} and $Ni-OH$ lattice vibrations respectively [37,38].

Electrochemical analysis

The electrochemical properties of the $Ni(OH)_2$ and $Ni(OH)_2$/GF electrodes were also probed in a 6.0 M KOH aqueous electrolyte using the three electrode configuration. CV characterization is useful in understanding the surface reactions of active material during different scan rate. Fig. 4a shows the CV curves of $Ni(OH)_2$ and $Ni(OH)_2$/GF electrodes at a sweep rate of 10 mV s^{-1}, which exhibits a pair of reversible redox peaks in the potential range of 0-0.5 mV s^{-1}, implying that the capacitance is governed by faradaic redox reactions. The anodic peak conformed to an

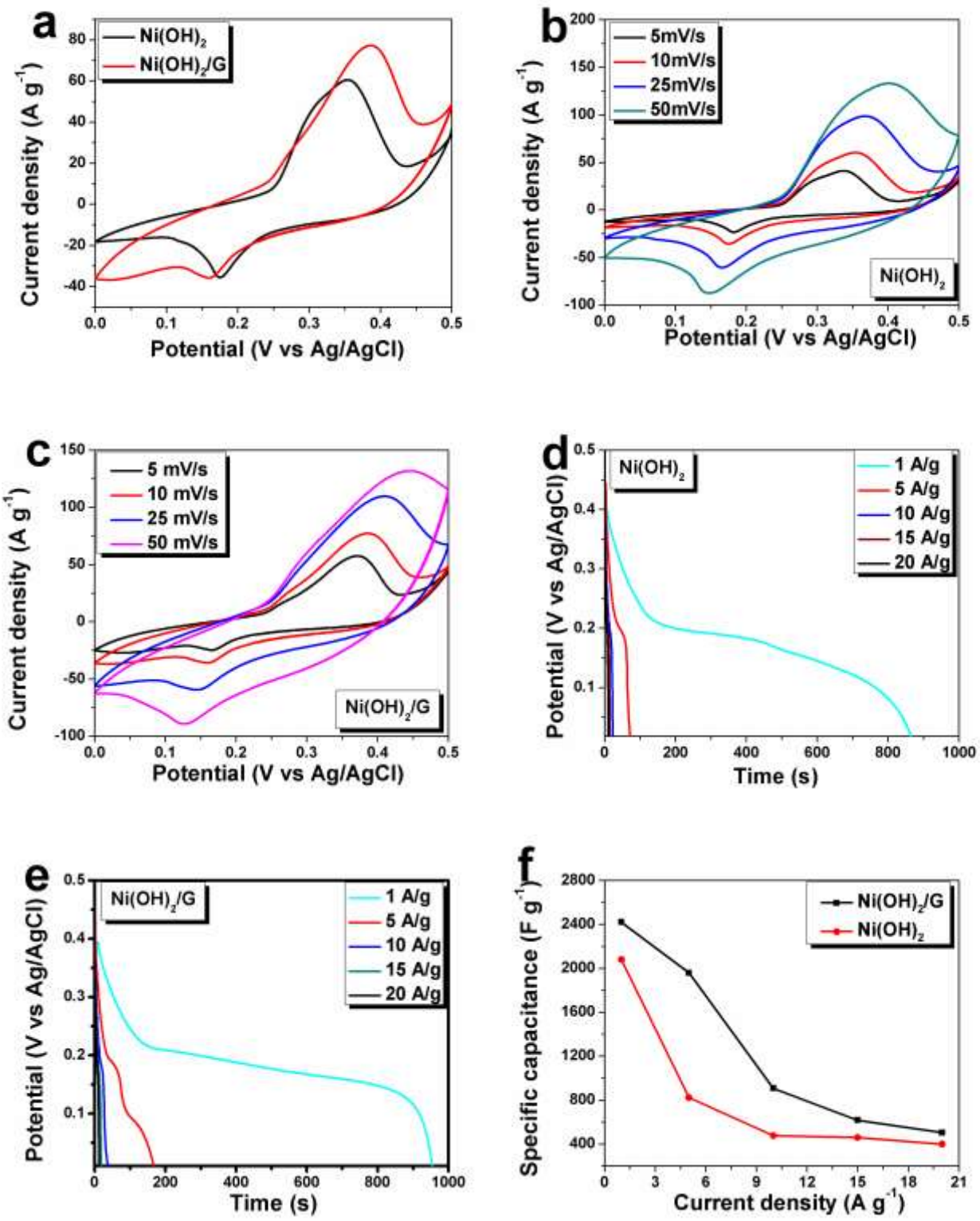

Fig. 4. CV of (a) Ni(OH)2 and Ni(OH)2/GF; (b) Ni(OH)2 and (c) Ni(OH)2/GF at different scan rates ranging from 5–50 mV s-1; CD of (d) Ni(OH)2 and (e) Ni(OH)2/GF measured at current densities of 1–20 A g-1; (f) specific capacitance of Ni(OH)2 and Ni(OH)2/GF electrode at different current densities calculated from the CD curves.

oxidation reaction of $Ni(OH)_2$ to NiOOH, and the cathodic peak showed the reverse process. The reaction process can be expressed as [39]:

$$Ni(OH)_2 + OH^- \longleftrightarrow NiOOH + H_2O + e^- \quad (5)$$

Fig. 4a clearly shows that $Ni(OH)_2$/GF has higher enclosed area, signifying its superior current response and thus its better electrochemical performance [40]. The improved performance could be due to the synergistic effect from the $Ni(OH)_2$ spheres added which prevents the restacking of the graphene sheet , therefore providing more surface area with higher electrolyte ion (K^+) accessibility as well as increase in the conductivity. From Fig. 4b-c, it is observed that as the scan rate increased, the potential of the anodic and cathodic peaks shifted in more positive and negative directions in the CV curves of $Ni(OH)_2$ and $Ni(OH)_2$/GF respectively at different scan rates ranging from 5-50 mV/s. This is due to the limitation of the ion diffusion rate to satisfy electronic neutralization during the redox reaction [41]. This also confirms that the electrochemical process is diffusion controlled as for faradaic process.

Fig 4d and e show the CD curves for $Ni(OH)_2$ and $Ni(OH)_2$/GF at different current densities of 1.0 – 20.0 A g^{-1}. The shape of the discharge curves indicate a characteristic faradaic behavior [42], which agrees well with the CV measurements that show redox peaks resulting from reaction at the electrode/electrolyte interface. Also higher discharge time at current density of 1 Ag^{-1} is observed in $Ni(OH)_2$/GF electrode (Fig. 4e). The specific capacitance was calculated from the CD curves using the following equation [43] :

$$C = {It}/{m\Delta V} \quad (6)$$

where I is a current (A), t is the discharge time (s), m is the mass of active material (g), and ΔV is the voltage range (V).

A specific capacitance of 2420 F g^{-1} was obtained for $Ni(OH)_2$/GF electrode compared with a value of 2080 F g^{-1} for pure $Ni(OH)_2$ electrode at a current density of 1 A g^{-1}. This increase in specific capacitance for the composite electrode is a direct consequent of the addition of the conductive and porous GF to the pristine $Ni(OH)_2$ providing an improved rate of electron transfer and also enhancing exfoliation of GF by $Ni(OH)_2$ particles which interact with graphene sheets, thus preventing the restacking of the graphene [32]. This result is higher than previously reported values for $Ni(OH)_2$/GF. For example, a specific capacitance of 1717 F g^{-1} at 0.5 A g^{-1} for ultra-small RGO-$Ni(OH)_2$ composites by Liu *et. al.* [4]. Similarly, Jiang *et. al.* reported $Ni(OH)_2$ nanoflakes on 3D graphene with a specific capacitance of 1450 F g^{-1} at 0.5 A g^{-1} [6], and Gu *et. al.* recorded a specific capacitance of 1724 F g^{-1} at 2 A g^{-1} obtained from $Ni(OH)_2$ deposited on the silicon carbide nanowires by electrochemical cathodic deposition [23].

Fig. 4f shows the plot of C vs current densities for both $Ni(OH)_2$ and $Ni(OH)_2$/GF electrodes. A decrease in specific capacitance with increasing current density is observed. This could be explained by the limited diffusion of ions at higher current densities, which could only reach the outer active surface of the electrode material for redox reactions [43].

The impedance spectra for $Ni(OH)_2$ and $Ni(OH)_2$/GF were analyzed using Nyquist plots to farther evaluate their electrochemical characteristics. The measurements were carried out in an open circuit (E_{oc}) potential and frequency range of 10 mHz to 100 kHz., The Nyquist plot presented in Fig. 5a shows the imaginary component (- Z'') of the impedance against the real component

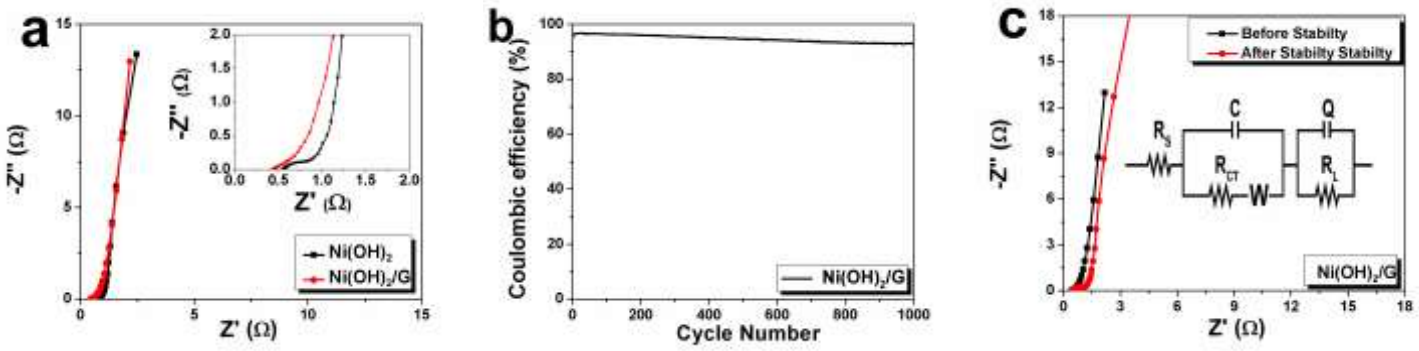

Fig. 5. (a) EIS plot of $Ni(OH)_2$ and $Ni(OH)_2$/GF (inset to the figure is the magnification of the high frequency region) (b) Coulombic efficiency for CD 1000 cycles for $Ni(OH)_2$/GF at a current density of 10 A g^{-1} (c) EIS plot of $Ni(OH)_2$/GF before and after cycling (inset to the figure is the equivalent circuit).

(Z'). Firstly, a partial semicircle is observed in the higher frequency region for $Ni(OH)_2$ electrode due to the dispersion effect [44], while the $Ni(OH)_2$/GF Nyquist plot shown no obvious semicircle, implying that $Ni(OH)_2$/GF has a very low charge transfer resistance (inset to Fig. 5a) [45]. In addition, the intersect on the real axis represents an equivalent series resistance (also known as solution resistance) R_s [46]. Thus, $Ni(OH)_2$ and $Ni(OH)_2$/GF have solution resistance values of around 0.56 Ω and 0.43 Ω, respectively. The lower R_s value obtained in $Ni(OH)_2$/GF electrode as compared to $Ni(OH)_2$ electrode could be due to the presence of the conductive graphene added in $Ni(OH)_2$ electrode. However, the Nyquist plot of $Ni(OH)_2$ and $Ni(OH)_2$/GF shows a line that deviated from the imaginary axis in the low frequency region, indicating an almost ideal capacitive behavior of the $Ni(OH)_2$ electrode and low ionic diffusion resistance in the electrode material [43].

Another very important characteristic to assess the electrochemical performance is the stability of the active material. Cyclic stability of $Ni(OH)_2$/GF electrode was investigated by CD at current density of 10 A g^{-1} for 1000 cycles (Fig. 5b). From the plot, an insignificant variation in the

coulombic efficiency ε (defined as $\varepsilon = t_c/t_d \times 100$, where $t_c \; and \; t_d$ are the charge and discharge time respectively) was observed from the continuous repetition of CD. Initially, ε increased for a small number of cycles to finally stabilize for higher number of cycles. This increase is due to the diffusion out of trapped ions between the $Ni(OH)_2$ crystalline layers during the hydrothermal reaction after activation of $Ni(OH)_2$[47]. After 1000 cycles of galvanostatic charge and discharge, ε of ~93% is recorded. This excellent stability demonstrated by $Ni(OH)_2$/GF electrode could be connected to the strong adhesion of $Ni(OH)_2$ on the surface of GF. Fig. 5c shows the Nyquist plots for the $Ni(OH)_2$/GF electrode before and after cycling. No significant increase in the R_S values was observed. However, an increase in the diameter of the partial semi-circular arc was observed after cycling which could be attributed to an increase in the charge transfer resistance (R_{CT}). The plots were further modeled with a (ZFIT) software that applies the complex nonlinear least-squares (CNLS) method. At the high frequency region, the equivalent circuit shown as inset to Figure 5c is a combination of the series resistance (R_S) which is in series with the charge transfer resistance (R_{CT}) and the Warburg and in parallel to the real capacitance (C). In the low frequency region, an ideal electrode should be a vertical line parallel to the imaginary axis with a mass capacitance denoted as (Q). The deviation from this ideal behavior is usually attributed to a leakage resistance R_L arising from the Faradaic charge transfer process, and this is always in parallel to the Q as shown in the equivalent circuit. Table 1 shows summary of the fitting parameters obtained before and after cycling from the

Table 1

Electrode	**R_S (Ω)**		**R_{CT} (Ω)**		**R_L(Ω)**	
$Ni(OH)_2$/GF	Before	After	Before	After	Before	After
	0.424	0.435	0.138	0.448	1.19	1.028

experimental impedance data. The values agree well with the observations made from the experiment with only a slight increase in the R_s value while the R_{CT} increases from 0.138 Ω before cycling to 0.448 Ω after cycling, thus showing that the model used for the fitting is reasonable. Furthermore, a leakage resistance which does not change significantly before and after cycling was observed. It is responsible to the deviation to the vertical line observed for ideal capacitor.

Conclusion

Summarily, an excellent and enhanced electrochemical behavior of $Ni(OH)_2$/GF electrode as compared to pristine $Ni(OH)_2$ electrode was reported in this work. The $Ni(OH)_2$ spheres were successfully produced via a facile hydrothermal reflux technique on a very conductive GF. The $Ni(OH)_2$/GF electrode exhibited better C of 2420 F g^{-1} at a current density of 1 A g^{-1} and have ε of ~ 93% after 1000 CD cycles. This indicates that this composite could be a potential electrode material for electrochemical application.

Acknowledgment

"This work is based on the research supported by the South African Research Chairs Initiative of the Department of Science and Technology and National Research Foundation of South Africa (Grant No 97994). Any opinion, finding and conclusion or recommendation expressed in this material is that of the author(s) and the NRF does not accept any liability in this regard". A. A. Khaleed acknowledges financial support from University of Pretoria and the NRF through SARChI in Carbon Technology and Materials.

References

1. Hu L, Yu Z, Hu Z, Song Y, Zhang F, Zhu H, Jiao S (2015) Facile synthesis of amorphous $Ni(OH)_2$ for high-performance supercapacitors via electrochemical assembly in a reverse micelle. Electrochim Acta 174:273–281.

2. Zhu G, Xi C, Shen M, Bao C, Zhu J (2014) Nanosheet-based hierarchical $Ni_2(CO_3)(OH_2)$ microspheres with weak crystallinity for high-performance supercapacitor. ACS Appl Mater Interfaces 6:17208–17214.

3. Zhou W, Cao X, Zeng Z, Shi W, Zhu Y, Yan Q, Liu H, Wang J, Zhang H (2013) One-step synthesis of Ni 3 S 2 nanorod@$Ni(OH)_2$ nanosheet core–shell nanostructures on a three-dimensional graphene network for high-performance supercapacitors. Energy Environ Sci 6:2216–2221.

4. Liu Y, Wang R, Yan X (2015) Synergistic Effect between Ultra-Small Nickel Hydroxide Nanoparticles and Reduced Graphene Oxide sheets for the Application in High-Performance Asymmetric Supercapacitor. Sci Rep 5:11095.

5. Yan J, Wang Q, Wei T, Fan Z (2014) Recent Advances in Design and Fabrication of Electrochemical Supercapacitors with High Energy Densities. Adv Energy Mater 4:1300816.

6. Jiang C, Zhao B, Cheng J, Li J, Zhang H, Tang Z, Yang J (2015) Hydrothermal synthesis of $Ni(OH)_2$ nanoflakes on 3D graphene foam for high-performance supercapacitors. Electrochim Acta 173:399–407.

7. Wu X, Xu A (2014) Carbonaceous hydrogels and aerogels for supercapacitors. J Mater Chem A 2:4852–4864.

8. Yan H, Bai J, Wang J, Zhang X, Wang B, Liu Q, Liu L (2013) Graphene homogeneously anchored with $Ni(OH)_2$ nanoparticles as advanced supercapacitor electrodes. CrystEngComm 15: 10007-10015.

9. Yang S, Gong Y, Liu Z, Zhan L, Hashim DP, Ma L, Vajtai R, Ajayan PM (2013) Bottom-up approach toward single-crystalline VO_2-graphene ribbons as cathodes for ultrafast lithium storage. Nano Lett 13:1596–1601.

10. Guo Y, Hu J, Wan L (2008) Nanostructured materials for electrochemical energy

conversion and storage devices. Adv Mater 20:2878–2887.

11. Wang W, Guo S, Lee I, Ahmed K, Zhong J, Favors Z, Zaera F, Ozkan M, Ozkan CS (2014) Hydrous ruthenium oxide nanoparticles anchored to graphene and carbon nanotube hybrid foam for supercapacitors. Sci Rep 4:4452.

12. Ji J, Zhang L, Ji H, Li Y, Zhao X, Bai X, Fan X, Zhang F, Rouff RS (2013) Nanoporous Ni $(OH)_2$ thin film on 3D ultrathin-graphite foam for asymmetric supercapacitor. ACS Nano 7:6237–6243.

13. Min S, Zhao C, Chen G, Qian X (2014) One-pot hydrothermal synthesis of reduced graphene oxide/$Ni(OH)_2$ films on nickel foam for high performance supercapacitors. Electrochim Acta 115:155–164.

14. Yan J, Sun W, Wei T, Zhang Q, Zhang Q, Wei F (2012) Fabrication and electrochemical performances of hierarchical porous $Ni(OH)_2$ nanoflakes anchored on graphene sheets. J Mater Chem 22:11494–11502.

15. Sun S, Lang J, Wang R, Kong L, Li X, Yan X (2014) Identifying pseudocapacitance of Fe_2O_3 in an ionic liquid and its application in asymmetric supercapacitors. J Mater Chem A 2:14550–14556.

16. Wu LC, Chen YJ, Mao ML, Li QH, Zhang M (2014) Facile Synthesis of Spike-Piece-Structured $Ni(OH)_2$ Interlayer Nanoplates on Nickel Foam as Advanced Pseudocapacitive Materials for Energy Storage. ACS Appl Mater Interfaces 6:5168–5174.

17. Dubal DP, Gund GS, Lokhande CD, Holze R (2013) Decoration of spongelike $Ni(OH)_2$ nanoparticles onto MWCNTs using an easily manipulated chemical protocol for supercapacitors. ACS Appl Mater Interfaces 5:2446–2454.

18. Wang H, Casalongue HS, Liang Y, Dai H (2010) $Ni(OH)_2$ nanoplates grown on graphene as advanced electrochemical pseudocapacitor materials. J Am Chem Soc 132:7472–7477.

19. Yan J, Fan Z, Sun W, Ning G, Wei T, Zhang Q, Zhang R, Zhi L, Wei F (2012) Advanced Asymmetric Supercapacitors Based on $Ni(OH)_2$/Graphene and Porous Graphene Electrodes with High Energy Density. Adv Funct Mater 22:2632–2641.

20. Dong X-C, Xu H, Wang X-W, Huang Y-X, Chan-Park MB, Zhang H, Wang L-H, Huang W,

Chen P (2012) 3D graphene-cobalt oxide electrode for high-performance supercapacitor and enzymeless glucose detection. ACS Nano 6:3206–3213.

21. Chen Z, Ren W, Gao L, Liu B, Pei S, Cheng HM(2011) Three-dimensional flexible and conductive interconnected graphene networks grown by chemical vapour deposition. Nat Mater 10:424–428.

22. Liu YF, Yuan GH, Jiang ZH, Yao ZP, Yue M (2015) Preparation of $Ni(OH)_2$-graphene sheet-carbon nanotube composite as electrode material for supercapacitors. J Alloys Compd 618:37–43.

23. Gu L, Wang Y, Lu R, Wang W, Peng X, Sha J (2015) Silicon carbide nanowires@ $Ni(OH)_2$ core–shell structures on carbon fabric for supercapacitor electrodes with excellent rate capability. J Power Sources 273:479–485.

24. Patil UM, Lee SC, Sohn JS, Kulkarni SV, Guravb KV, Kimb JH, Kimc JH, Leec S, Jun SC (2014) Enhanced Symmetric Supercapacitive Performance of $Co(OH)_2$ Nanorods Decorated Conducting Porous Graphene Foam Electrodes. Electrochim Acta 129:334–342.

25. Bello A, Makgopa K, Fabiane M, Dodoo-Ahrin D, Ozoemena KI, Manyala N (2013) Chemical adsorption of NiO nanostructures on nickel foam-graphene for supercapacitor applications. J Mater Sci 48:6707–6712.

26. Ferrari A (2007) Raman spectroscopy of graphene and graphite: disorder, electron–phonon coupling, doping and nonadiabatic effects. Solid State Commun 143:47–57.

27. Cai F-S, Zhang G-Y, Chen J, Gou X-L, Liu H-K, Dou S-X (2004) $Ni(OH)_2$ tubes with mesoscale dimensions as positive-electrode materials of alkaline rechargeable batteries. Angew Chem Int Ed Engl 43:4212–4216.

28. Jiang H, Zhao T, Li C, Ma J (2011) Hierarchical self-assembly of ultrathin nickel hydroxide nanoflakes for high-performance supercapacitors. J Mater Chem 21:3818–3823.

29. Chae SJ, Gunes F, Kim KK, Kim ES, Han GH, Kim SM, Shin H-J, Yoon S-M, Choi J-Y, Park MH, Yang CW, Pribat D, Lee YG (2009) Synthesis of large-area graphene layers on poly-nickel substrate by chemical vapor deposition: wrinkle formation. Adv Mater 21:2328–2333.

30. Lee J, Ahn T, Soundararajan D (2011) Non-aqueous approach to the preparation of reduced graphene oxide/α-$Ni(OH)_2$ hybrid composites and their high capacitance behavior. Chem commun 47:6305–6307.

31. Bragg WL (1913) The diffraction of short electromagnetic waves by a crystal. In: Proc. Camb. Philol. Soc. 43–57

32. Momodu D, Barzegar F, Bello A, Dangbegnon J, Masikhwa T, Madito J, Manyala N (2015) Simonkolleite-graphene foam composites and their superior electrochemical performance. Electrochim Acta 151:591–598.

33. Yang S, Wu X, Chen C, Dong H, Hu W, Wang X (2012) Spherical α-$Ni(OH)_2$ nanoarchitecture grown on graphene as advanced electrochemical pseudocapacitor materials. Chem Commun 48:2773–2775.

34. Nethravathi C, Rajamathi M (2008) Chemically modified graphene sheets produced by the solvothermal reduction of colloidal dispersions of graphite oxide. Carbon 46:1994–1998.

35. Xu L, Ding Y, Chen C, Zhao L (2007) 3D flowerlike α-nickel hydroxide with enhanced electrochemical activity synthesized by microwave-assisted hydrothermal method. Chem mater 20:308–316.

36. Tessier C, Guerlou-Demourgues L (2000) Structural study of zinc-substituted nickel hydroxides. J Mater Chem 10:1185–1193.

37. Ren Y, Gao L (2010) From Three-Dimensional Flower-Like α-$Ni(OH)_2$ Nanostructures to Hierarchical Porous NiO Nanoflowers: Microwave-Assisted Fabrication and Supercapacitor Properties. J Am Ceram Soc 93:3560–3564.

38. Liu X, Yu L (2004) Synthesis of nanosized nickel hydroxide by solid-state reaction at room temperature. Mater Lett 58:1327–1330.

39. Han D, Xu P, Jing X, Wanga J, Yang P, Shen Q, Liu J, Song D, Gao Z, Zhang M (2013) Trisodium citrate assisted synthesis of hierarchical NiO nanospheres with improved supercapacitor performance. J Power Sources 235:45–53.

40. Cheng H, Su A, Li S, Nguyen ST, Lu L, Lim CYH, Duong HM (2014) Facile synthesis and advanced performance of $Ni(OH)_2$/CNTs nanoflake composites on supercapacitor applications. Chem Phys Lett 601:168–173.

41. Lee JW, Ahn T, Kim JH, Ko JM, Kim J-D (2011) Nanosheets based mesoporous NiO microspherical structures via facile and template-free method for high performance supercapacitors. Electrochim Acta 56:4849–4857.

42. Simon P, Gogotsi Y, Dunn B (2014) Where do batteries end and supercapacitors begin? Sci Mag 343:1210–1211.

43. Yang W, Gao Z, Wang J, Ma J, Zhang M, Liu L (2013) Solvothermal one-step synthesis of Ni-Al layered double hydroxide/carbon nanotube/reduced graphene oxide sheet ternary nanocomposite with ultrahigh capacitance for supercapacitors. ACS Appl Mater Interfaces 5:5443–5454.

44. Wang B, Liu Q, Qian Z, Zhang X, Wang J, Li Z, Yan H, Gao Z, Zhao F, Liu L (2014) Two steps in situ structure fabrication of Ni–Al layered double hydroxide on Ni foam and its electrochemical performance for supercapacitors. J Power Sources 246:747–753.

45. Wang L, Li X, Guo T, Yan X, Tay BK (2014) Three-dimensional $Ni(OH)_2$ nanoflakes/graphene/nickel foam electrode with high rate capability for supercapacitor applications. Int J Hydrogen Energy 39:7876–7884.

46. Fan Z, Yan J, Wei T, Zhi L (2011) Asymmetric supercapacitors based on graphene/MnO_2 and activated carbon nanofiber electrodes with high power and energy density. Adv Funct Mater 21:366–2375.

47. Yuan C, Zhang X, Su L, Gao B, Shen L (2009) Facile synthesis and self-assembly of hierarchical porous NiO nano/micro spherical superstructures for high performance supercapacitors. J Mater Chem 19:5772–5777.